Nano Research
2022, 15(3): 1803–1808

ISSN 1998-0124 CN 11-5974/O4
https://doi.org/10.1007/s12274-021-3748-6

Research Article

Atomic CoN_3S_1 sites for boosting oxygen reduction reaction via an atomic exchange strategy

Qianjun Zhi, Rong Jiang, Wenping Liu, Tingting Sun, Kang Wang (✉), and Jianzhuang Jiang (✉)

Beijing Advanced Innovation Center for Materials Genome Engineering, Beijing Key Laboratory for Science and Application of Functional Molecular and Crystalline Materials, Department of Chemistry and Chemical Engineering, School of Chemistry and Biological Engineering, University of Science and Technology Beijing, Beijing 100083, China

Received: 3 June 2021 / **Revised:** 12 July 2021 / **Accepted:** 14 July 2021

ABSTRACT

It is vitally important to develop high-efficiency low-cost catalysts to boost oxygen reduction reaction (ORR) for renewable energy conversion. Herein, an A-CoN_3S_1@C electrocatalyst with atomic CoN_3S_1 active sites loaded on N, S-codoped porous carbon was produced by an atomic exchange strategy. The constructed A-CoN_3S_1@C electrocatalyst exhibits an unexpected half-wave potential (0.901 V vs. reversible hydrogen electrode) with excellent durability for ORR under alkaline conditions (0.1 M KOH), superior to the commercial platinum carbon (20 wt.% Pt/C). The outstanding performance of A-CoN_3S_1@C in ORR is due to the positive effect of S atoms doping on optimizing the electron structure of the atomic CoN_3S_1 active sites. Moreover, the rechargeable zinc-air battery in which both A-CoN_3S_1@C and IrO_2 were simultaneously served as cathode catalysts (A-CoN_3S_1@C &IrO_2) exhibits higher energy efficiency, larger power density, as well as better stability, compared to the commercial Pt/C&IrO_2-based zinc-air battery. The present result should be helpful for developing lower cost and higher performance ORR catalysts which is expected to be used in practical applications in energy devices.

KEYWORDS

atomic sites, oxygen reduction reaction, CoN_3S_1, zinc-air battery

1 Introduction

Oxygen reduction reaction (ORR), which possesses wide application demand in fuel cell and metal-air cell, has been extensively studied recently [1, 2]. The nanomaterials based on platinum are the most effective catalysts towards ORR [3, 4]. Nevertheless, the high cost and scarcity of Pt-based catalysts seriously impede their wide range of applications [5–7]. As a result, it is significantly important and highly urgent to develop high-efficiency low-cost alternatives of Pt-based catalysts to boost ORR. Up to now, various non-noble metal electrocatalysts with ORR activity have been developed including carbon materials [8], perovskites [9, 10], transition-metal oxides [11, 12], sulfides [13], and nitrides [14–16]. Among these developed catalysts, Co-N-C catalysts with distributed atomically Co-N_x active sites on carbon supports have attracted great attentions owing to their excellent activity, super stability, and maximum utilization of metal atoms [17–19]. However, the catalytic performance of atomic Co-N-C electrocatalysts for ORR is still not as good as the state-of-the-art electrocatalysts based on non-precious metal such as Fe-based atomic catalysts (Fe-N-C catalysts) [20–24], which limits the overall functional performance and restricts the practical application.

It has been found that S doping is an alternative method to improve the catalytic performance by tuning the electronic structure of the center of catalytic activity in M-N-C catalyst [25, 26]. For instance, Zhu et al. investigated electrocatalytic activity of porous S-doped nanosheets based on atomic Fe catalysts (Fe-N-C), demonstrating that the involvement of S element in atomically dispersed Fe-N_x species played a vital role in enhancing the activities of ORR and oxygen evolution reaction (OER) [27]. Li et al. developed Cu-based catalyst S-Cu-ISA/SNC with atomically dispersed Cu atoms bonded with both nitrogen and sulfur atoms, which demonstrated that enhanced ORR electroatalytic performance along with an excellent $E_{1/2}$ of 0.918 V (vs. RHE) under alkaline condition was owing to the local structure regulation by doping sulfur atoms into a varity of materials [28]. However, the effect of direct engagement of Co and S atoms on the functional performance of the atomic CoN_xS_y catalysts towards ORR has been rarely investigated. Herein, we report an atomic A-CoN_3S_1@C electrocatalyst with atomic CoN_3S_1 sites involved in an N, S-codoping porous carbon by an atomic exchange strategy. A-CoN_3S_1@C exhibits an outstanding $E_{1/2}$ of 0.901 V vs. RHE) for ORR as well as good stability in alkaline electrolyte solution, causing A-CoN_3S_1@C to becoming one of the best-performing ORR electrocatalysts based on non-precious-metal. The present result should be helpful for developing lower cost and higher performance of oxygen catalysts with various applications.

2 Experimental method

2.1 Preparing method of A-CoN_4@C

In a typical synthesis, the mixture of commercial BP 2000 (200 mg), 4-nitrophtalonitrile (40 mg), and $CoCl_2{\cdot}6H_2O$ (20 mg) was added into a 70 mL mixed solvent of ethanol and acetone

Address correspondence to Kang Wang, kangwang@ustb.edu.cn; Jianzhuang Jiang, jianzhuang@ustb.edu.cn

(1:6). The suspension was treated with ultrasound for 1 h and then stirred vigorously until the liquid was completely volatilized. The obtained black powder (200 mg) was transferred into a porcelain boat and then heated respectively at 250 and 800 °C for 120 min under an inert atmosphere (N_2) in tube furnace. The heating rate is 3 °C/min. The black powder was then pickled in acid aqueous solution (0.5 M HCl) at the temperature of 80 °C for six hours. The product was separated by filtration, washed with pure water for three times to neutral. Finally, the residual solvent is removed by drying at 80 °C for 20 h in vacuum, generating A-CoN_4@C (ca. 180 mg).

2.2 Preparing method of A-CoN_3S_1@C

For the production purposes of A-CoN_3S_1@C, both powdered sulfur (250 mg) and above-mentioned A-CoN_4@C (50 mg) are firstly placed on each end of the porcelain boat. The porcelain boat containing the two reactants is then heated in a tubular furnace at 700 °C for 2 h under an inert atmosphere (N_2). The heating rate is 3 °C/min. The black powder was carefully washed by water to neutral. Finally, the residual solvent in the sample is removed by drying at 80 °C for 20 h in vacuum, generating the target material of A-CoN_3S_1@C (ca. 45 mg).

2.3 Preparing method of N/S/C

Following above-described preparing method of A-CoN_4@C without the addition of $CoCl_2{\cdot}6H_2O$, the metal-free sample N/C was prepared. Then N/C (50 mg) and powdered sulfur (250 mg) are placed on each end of the porcelain boat. The porcelain boat containing the two reactants is then heated at 700 °C for 2 hours under an inert atmosphere (N_2) in a tubular furnace. In order to eliminate the influence of pickling treatment on the controlled sample (N/S/C), the black powder was then pickled in acid aqueous solution (0.5 M HCl) at the temperature of 80 °C for 6 h. The resulting powder was black, and then was carefully washed by pure water to neutral. Finally, the residual solvent in the sample is removed by drying at the temperature of 80 °C for 20 h in vacuum, generating N/S/C (ca. 45 mg).

3 Results and discussion

3.1 Synthesis and characterization

A-CoN_3S_1@C was prepared by a facile atomic exchange strategy, as illustrated in Fig. 1 and detailed in Experimental Method section. The Co-N_x precursor was first anchored into commercial porous carbon BP 2000 by annealing of the mixture of

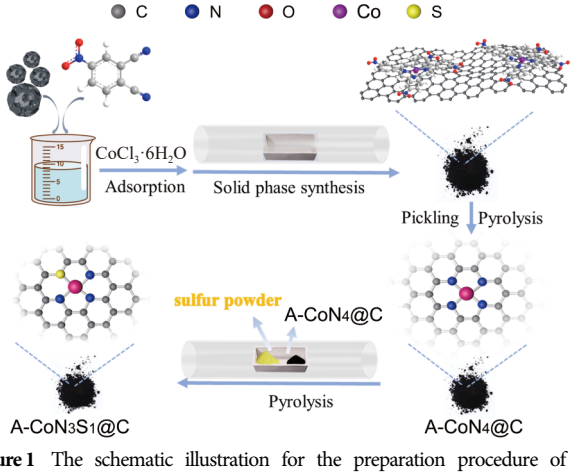

Figure 1 The schematic illustration for the preparation procedure of A-CoN_3S_1@C (gray: carbon; blue: nitrogen; red: oxygen; purple: cobalt; yellow: sulfur).

$CoCl_2{\cdot}6H_2O$, 2,4-nitrophtalonitrile, and BP 2000 through the heating at 250 °C for 2 h and then at higher temperature of 800 °C for another 2 h, which generated A-CoN_4@C with atomically dispersed Co-N_4 moieties. Then, A-CoN_4@C was further annealed at 900 °C in the presence of sulfur powder. In this process, a part of N atoms including Co-N species are removed through heat treatment [29], resulting in various vacancies on porous carbon, while S atoms are integrated into these vacancies, forming A-CoN_3S_1@C with CoN_3S_1 structure. For the purpose of comparison, the metal-free sample (marked as N/S/C) was produced by the same process without adding $CoCl_2{\cdot}6H_2O$. The content of cobalt in A-CoN_3S_1@C is determined as ca. 0.98 wt.% by the measurement of inductively coupled plasma-atomic emission spectroscopy (ICP-AES), respectively. The transmission electron microscopy (TEM) was used to characterize the nanostructures of A-CoN_3S_1@C, Fig. 2(a) and Fig. S1 in the Electronic Supplementary Material (ESM)), which reveals that A-CoN_3S_1@C inherit the original BP structure. Furthermore, the N_2 adsorption measurement at 77 K shows a Brunauer-Emmett-Teller (BET) specific surface area of 741 m^2/g for A-CoN_3S_1@C (Fig. S2 in the ESM), which is in favour of the charge and mass transportation during electrochemical reactions [30]. The aberration-corrected atomic-resolution high angle annular dark-field scanning transmission electron microscopy (HAADF-STEM) measurements were further utilized for testifying the existed form of atomic cobalt species in the sample of A-CoN_3S_1@C. As displayed in Figs. 2(b) and 2(c), high-density bright dots with the average size of ca. 0.25 nm were obviously picked out on the surface of A-CoN_3S_1@C, corresponding to Co atoms. This result indicates the atomic distribution of Co atoms in A-CoN_3S_1@C. Moreover, the analysis result of elemental mappings shows the homogeneous spatial distribution of each elemental throughout A-CoN_3S_1@C, Fig. 2(d). In addition, the analysis result of X-ray diffraction (XRD) pattern exhibits that there is no characteristic peak belong to Co metal from Fig. S2 in the ESM. Therefore, we can draw inferences that the metal-related particles are absent and confirm the atomic distribution nature of cobalt element in A-CoN_3S_1@C electrocatalysts. The ratio between the D and G bands (I_D/I_G) is as large as 1.21 for BP 2000 as received by Raman spectrum, Fig. S5 in the ESM, revealing abundant defects on BP 2000 which could serve as trapping sites for the atomic Co element. Nevertheless, after the annealing treatment for doping Co, the value of I_D/I_G of the A-CoN_3S_1@C catalyst decreases to 1.15, suggesting the increased graphitization degree of the A-CoN_3S_1@C catalyst, in favour of the electronic transmission during electrocatalytic process [31]. In addition, similar to A-CoN_3S_1@C catalyst, the A-CoN_4@C with a cobalt content of 1.1 wt.% also shows a large BET surface area of 847 m^2/g and equally distributed atomic Co species, Figs. S1–S5 in the ESM.

The chemical states and bonding configuration of the atoms of A-CoN_3S_1@C were explored by X-ray photoelectron spectroscopy (XPS). As shown in Fig. 3(a) and Fig. S6 in the ESM, these high-resolution spectra for N 1s of A-CoN_3S_1@C and A-CoN_4@C in our study can be divided into five peaks at 398.8, 399.5, 399.9, 400.8, and 402.2 eV, which correspond to the pyridine N, metal-N, pyrrole N, graphite N, and oxidized N, respectively [32]. The fact that metal-N peaks exists in A-CoN_3S_1@C and A-CoN_4@C suggests the Co-N_x configuration in Co-based samples. Figure 3(b) shows the high-resolution XPS spectra for S 2p of N/S/C and A-CoN_3S_1@C. As can be found, besides the peaks due to thiophene S (163.1 and 164.1 eV) and C-SO_x-C (166.5 eV) in both two samples, one peak at 162.3 eV assigned to Co-S was also observed for A-CoN_3S_1@C, implying that S atoms have been successfully doped into the carbon skeleton and Co-S_x configuration exists in A-CoN_3S_1@C. Furthermore, A-CoN_3S_1@C

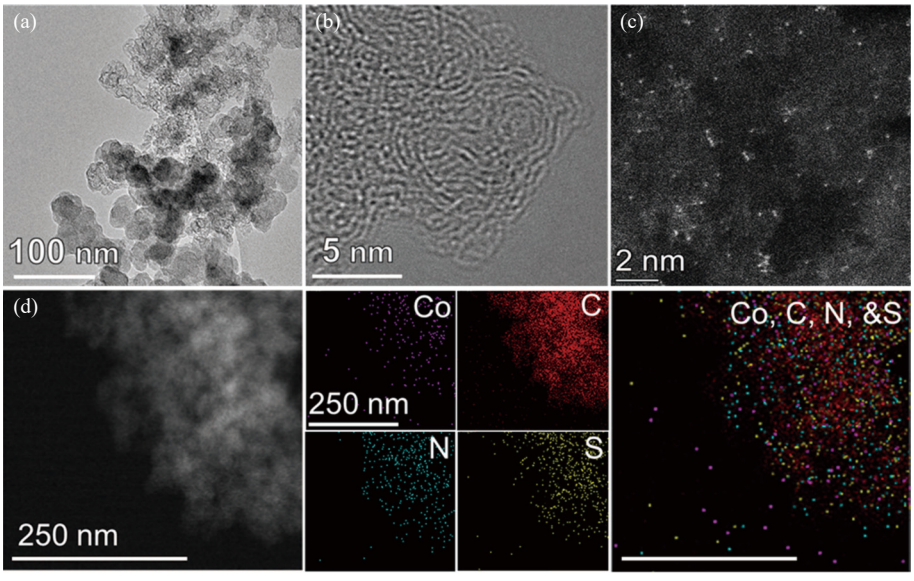

Figure 2 (a) TEM, (b) high-resolution TEM, and (c) HAADF-STEM images of A-CoN_3S_1@C. (d) Elemental mapping images of A-CoN_3S_1@C.

exhibits two peaks assigned to Co $2p_{3/2}$ (782.2 eV) and Co $2p_{1/2}$ (798.6 eV) [33] in the high-resolution Co 2p spectra, which are negatively shift comparing with those of A-CoN_4@C, Fig. 3(c), revealing the effect of the coordination of S atoms on modulating the electron structure of the atomic Co sites. Additionally, it is worth noting that we also prepared the sample A-CoN@N/S/C by using one-step pyrolysis with the detailed preparing method shown in the supplementary material. As shown in Fig. S6 in the ESM, A-CoN@N/S/C exhibits a much weaker Co-S peak with much worse ORR activity compared to A-CoN_3S_1@C. These results confirm that the atomic exchange strategy used for the synthesis of A-CoN_3S_1@C is effective for the formation of the Co-S bond.

X-ray absorption near-edge structure (XANES) and extended X-ray absorption fine structure (EXAFS) spectroscopy were used to further determine the chemical state and local coordination environment of the Co species. As shown in Fig. 3(d), the Co K-edge XANES spectra exhibit that the absorption edge for both A-CoN_3S_1@C and A-CoN_4@C locates similarly as CoPc, demonstrating the average oxidation state of Co atoms in both samples are close to +2. Noted, A-CoN_3S_1@C displays the pre-edge peak at 7,725 eV, which is larger than that of A-CoN_4@C (7,722 eV), indicting the oxidization state of Co shifts to a larger value after S doping. These results further suggest the S doping enable to modulate the electron structure of the atomic Co-N sites, in line with the XPS results. The coordination environment around Co atoms was further analyzed by using Fourier-transformed (FT) EXAFS spectra. As can be seen in Fig. 3(e), both A-CoN_3S_1@C and A-CoN_4@C exhibit respectively scattering path of Co-N bond with a peak at ca. 1.41 and 1.47 Å. At the same time, the signal for Co-Co bond at ca. 2.21 Å is not observed, which indicates the atomically dispersed nature of the Co species in these two samples. It is worth noting that a peak at ca. 1.83 Å is also observed in the FT EXAFS spectrum of the A-CoN_3S_1@C electrocatalyst, which is assigned to the Co-S scattering path, confirming the coordination between Co and S atoms in the A-CoN_3S_1@C electrocatalyst. Moreover, the EXAFS fitting results suggest a CoN_3S_1 coordination structure (three Co–N bonds and one Co–S bond) for A-CoN_3S_1@C while a Co-N_4 coordination structure for A-CoN_4@C, Fig. 3(f), and Figs. S7 and S8 and Table S1 in the ESM. The aforementioned results demonstrate that the incorporating S changes the local coordination structure of the

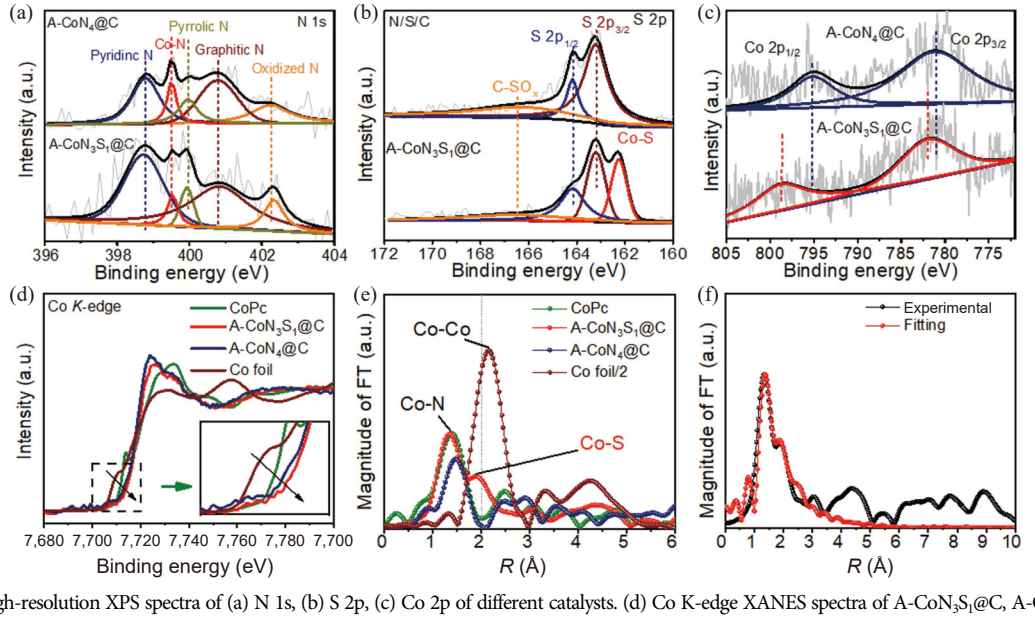

Figure 3 The high-resolution XPS spectra of (a) N 1s, (b) S 2p, (c) Co 2p of different catalysts. (d) Co K-edge XANES spectra of A-CoN_3S_1@C, A-CoN_4@C, Co foil, and CoPc. (e) k^3-weighted EXAFS spectra of CoPc, Co foil, A-CoN_4@C and A-CoN_3S_1@C. (f) The EXAFS fitting results of A-CoN_3S_1@C at *R* space.

atomic Co species and in turn modulates the electron structure of the atomic Co sites in the A-CoN_3S_1@C electrocatalyst, which significantly affects the electrocatalytic activity as detailed below.

3.2 Electrocatalytic performance

A typical measurement of a rotating disk electrode (RDE) in O_2-saturated 0.1 M KOH electrolyte was performed to access the catalytic activity of the A-CoN_3S_1@C electrocatalyst [34]. For the purpose of comparison, the electrocatalytic activities of A-CoN_4@C, N/S/C, and commercial Pt/C (20 wt.%) were also studied in exactly the same experimental situation. As shown in Fig. 4(a), linear sweep voltammetry (LSV) curves display that the A-CoN_3S_1@C electrocatalyst explores an E_{onset} of 1.001 mV vs. RHE, an $E_{1/2}$ of 0.901 V vs. RHE, and a J_L of –5.81 mA/cm^2. Figure 4(a) also exhibits the LSVs of controlled samples (A-CoN@N/S/C, N/S/C and A-CoN_4@C). The E_{onset} and $E_{1/2}$ of the N/S/C sample are 0.79 and 0.60 V vs. RHE, respectively, which are significantly inferior to those of A-CoN_3S_1@C, revealing that the atomically dispersed CoN_3S_1 moieties are the active centers of A-CoN_3S_1@C. Moreover, we can also see that A-CoN_3S_1@C exhibit enhanced ORR activity in comparison with A-CoN_4@C (Figs. 4(a) and 4(b)), implying the effect of the doping of S atoms and CoN_3S_1 moieties though modulating the electron structure of the atomic Co sites on improving the ORR electrotic activity. Particularly, while the E_{onset} and J_L of A-CoN_3S_1@C are similar to Pt/C, the $E_{1/2}$ of A-CoN_3S_1@C is even 54 mV higher than that of 20% Pt/C ($E_{1/2}$ = 0.847 V vs. RHE), indicating the excellent ORR activity of A-CoN_3S_1@C. In addition, as shown in Fig. S9 in the ESM, the value of Tafel slope of A-CoN_3S_1@C is only 57 mV/dec, even smaller than that of 20% Pt/C, suggesting the faster kinetics of A-CoN_3S_1@C. We also compare the $E_{1/2}$ of A-CoN_3S_1@C with the state-of-the-art ORR electrocatalysts based on the non-precious-metal. As detailed in Table S2 in the ESM, A-CoN_3S_1@C surpasses all the thus far reported Co based catalysts and is comparable to the Fe-N-C catalysts in the same situation.

These LSV curves were recorded under the rotation rate in the range from 400 to 2,500 rpm to further understand the ORR catalytic performance of the A-CoN_3S_1@C electrocatalyst, Fig. 4(d). On the basis of the Koutecky-Levich (K-L) plots, the electron-transfer number (n) for A-CoN_3S_1@C was calculated as 3.95, 3.97, and 3.99 at 0.5, 0.6, and 0.7 V vs. RHE, respectively, which is similar to the 20% Pt/C, exploring an efficient 4e$^-$ reduction process. The n of A-CoN_3S_1@C was further determined though the RRDE test, Fig. 4(e), which reveals n > 3.85 between 0.3–0.9 V (vs. RHE) on the A-CoN_3S_1@C electrode, in line with the RDE result. Furthermore, the peroxide yield of the A-CoN_3S_1@C electrocatalyst is below 3.0% in the potential range from 0.3 to 0.9 V (vs. RHE), further confirming the high selectivity of A-CoN_3S_1@C towards ORR.

In a practical application, the durability is also extremely significant for the ORR catalysts, which was first investigated by accelerated stress tests (AST) in 0.1 M KOH. As displayed in Fig. 4(e) and Fig. S8 in the ESM, after 5,000 cycling tests of cyclic voltammetry (CV) in the potential range from 0.6 to 1.1 V (vs. RHE), the $E_{1/2}$ of the A-CoN_3S_1@C electrocatalyst decreased by only 3 mV, which is less than that of commercial Pt/C (20%) (35 mV), suggesting the superior stability of the A-CoN_3S_1@C electrocatalyst to the Pt/C catalyst. Furthermore, the A-CoN_3S_1@C electrocatalyst retains a high relative current of 95% after scanning 20,000 s in the i–t test, which is higher than that of 79% for Pt/C (20%), Fig. 4(e) and Fig. S9 in the ESM, further confirming the

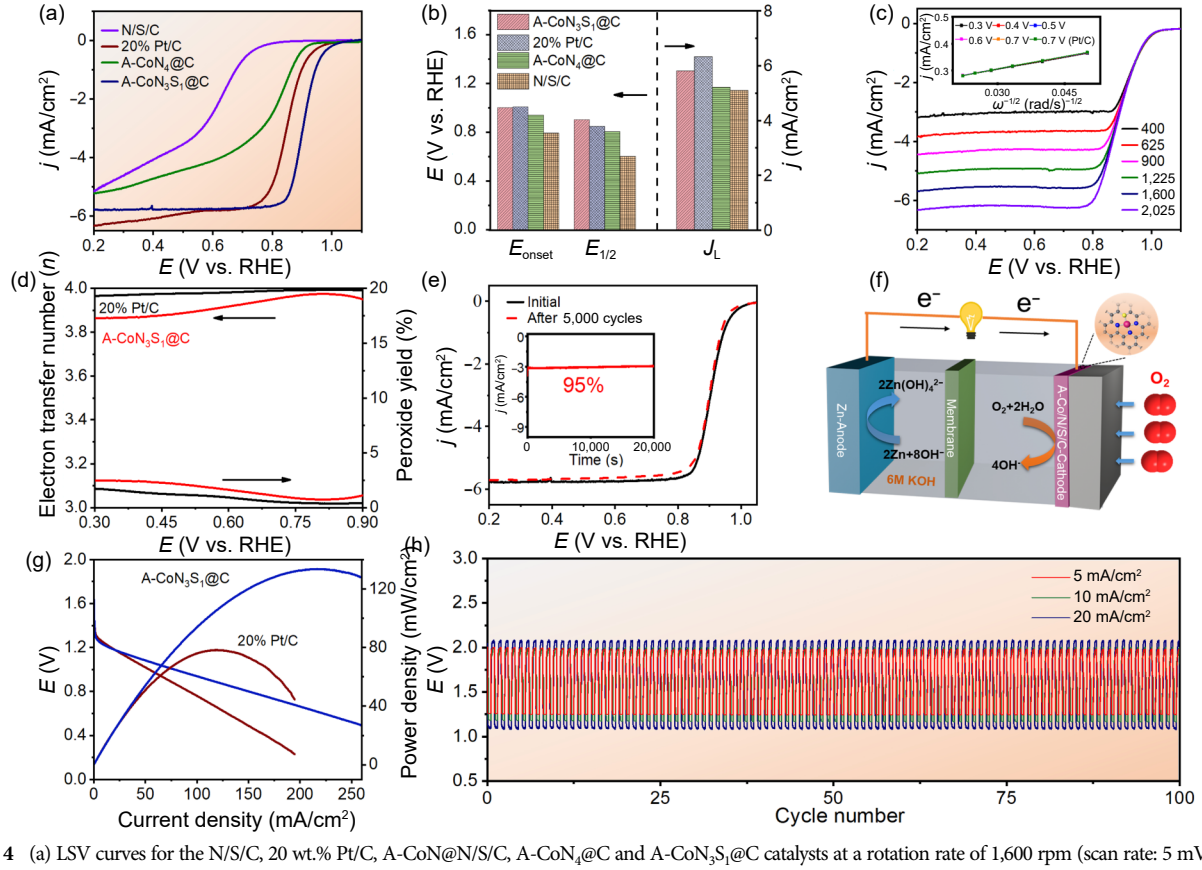

Figure 4 (a) LSV curves for the N/S/C, 20 wt.% Pt/C, A-CoN@N/S/C, A-CoN_4@C and A-CoN_3S_1@C catalysts at a rotation rate of 1,600 rpm (scan rate: 5 mV/s). (b) Comparison of E_{onset}, $E_{1/2}$ and J_L among samples in this work. (c) LSV curves of A-CoN_3S_1@C at various rotation rates (400–2,025 rpm). The inset shows K–L plots of A-CoN_3S_1@C at various potentials. (d) H_2O_2 yield and electron transfer number of A-CoN_3S_1@C and Pt/C (20%). (e) LSV curves of A-CoN_3S_1@C before and after 5,000 cycles. The inset shows chronoamperometry curve for A-CoN_3S_1@C. (f) Schematic of the rechargeable Zn–air battery. (g) Discharge polarization curves and corresponding power density plots. (h) Charge and discharge cycling curves of A-CoN_3S_1@C based on the Zn–air battery at a constant charge–discharge current density of 5, 10, and 20 mA/cm^2 (600 s for every cycle).

higher stability of A-CoN_3S_1@C. Besides, the morphology of A-CoN_3S_1@C after stability test is also retained, Fig. S10 in the ESM.

Inspired by the high performance of A-CoN_3S_1@C towards ORR, the composite material of IrO_2 and A-CoN_3S_1@C (A-CoN_3S_1@C &IrO_2) was served as the cathode catalyst to access its potential application in rechargeable Zn-air batteries under realistic conditions, Fig. 4(f). Under the same testing conditions, the 20% Pt/C&IrO_2 combination was also integrated into a rechargeable zinc-air battery for comparison. As displayed in Fig. 4(g) and Fig. S11 in the ESM, the open circuit voltage of A-CoN_3S_1@C &IrO_2-based Zn-air battery is 1.43 V, which are higher than that for the Pt/C&IrO_2-based Zn-air battery (1.32 V). In addition, A-CoN_3S_1@C &IrO_2-based Zn-air battery also exhibits a larger peak power density of 135 mW/cm^2 at 224 mA/cm^2 than that of Pt/C&IrO_2-based Zn-air battery which shows the maximum power density of ≈ 80 mW/cm^2. Besides, the cycling measurements of Zn–air battery based on A-CoN_3S_1@C &IrO_2 were performed at 5, 10, and 20 mA/cm^2 to evaluate the corresponding rechargeability, which displayed impressively negligible potential fading after 100 cycle tests (Fig. 4(h)), better than that of Pt/C &IrO_2 (Fig. S12 in the ESM). All aforementioned results declare the great application potential of the as-prepared A-CoN_3S_1@C catalyst in the domain of energy conversion and storage devices.

4 Conclusion

In summary, we have prepared an atomic A-CoN_3S_1@C electrocatalyst with atomically CoN_3S_1 active sites which are supported on N, S co-doping porous carbon material by an atomic exchange strategy. The constructed A-CoN_3S_1@C catalyst diaplays enhanced ORR performance under alkaline condition, even overmatching the commercial Pt/C (20 wt.%). This exceedingly great ORR activity of A-CoN_3S_1@C was owing to the atomically dispersed CoN_3S_1 active centers as well as the excellent effect of doping of S atoms on optimizing the electron structure of the atomic Co sites. Moreover, we also demonstrate that A-CoN_3S_1@C is a promising candidate as the air electrode catalyst in rechargeable zinc-air batteries. The present result should be helpful for developing lower cost and higher performance of oxygen catalysts with practical application in energy devices.

Acknowledgements

Financial support from the Natural Science Foundation of China (Nos. 21631003 and 21871024), the Fundamental Research Funds for the Central Universities (Nos. FRF-BR-19-003B and FRF-BD-20-14A).

Electronic Supplementary Material: Supplementary material (experimental section and supplementary figures and tables) is available in the online version of this article at https://doi.org/10.1007/s12274-021-3748-6.

References

[1] Chu, S.; Majumdar, A. Opportunities and challenges for a sustainable energy future. *Nature* **2012**, *488*, 294–303.

[2] Kulkarni, A.; Siahrostami, S.; Patel, A.; Nørskov, J. K. Understanding catalytic activity trends in the oxygen reduction reaction. *Chem. Rev.* **2018**, *118*, 2302–2312.

[3] Liu, J.; Jiao, M. G.; Lu, L. L.; Barkholtz, H. M.; Li, Y. P.; Wang, Y.; Jiang, L. H.; Wu, Z. J.; Liu, D. J.; Zhuang, L. et al. High performance platinum single atom electrocatalyst for oxygen reduction reaction. *Nat. Commun.* **2017**, *8*, 15938.

[4] Liu, J.; Jiao, M. G.; Mei, B. B.; Tong, Y. X.; Li, Y. P.; Ruan, M. B.; Song, P.; Sun, G. Q.; Jiang, L. H.; Wang, Y. et al. Carbon-supported divacancy-anchored platinum single-atom electrocatalysts with superhigh Pt utilization for the oxygen reduction reaction. *Angew. Chem., Int. Ed.* **2019**, *58*, 1163–1167.

[5] Zhao, Z. P.; Chen, C. L.; Liu, Z. Y.; Huang, J.; Wu, M. H.; Liu, H. T.; Li, Y. J.; Huang, Y. Pt-based nanocrystal for electrocatalytic oxygen reduction. *Adv. Mater.* **2019**, *31*, 1808115.

[6] Zhao, Z. H.; Li, M. T.; Zhang, L. P.; Dai, L. M.; Xia, Z. H. Design principles for heteroatom-doped carbon nanomaterials as highly efficient catalysts for fuel cells and metal–air batteries. *Adv. Mater.* **2015**, *27*, 6834–6840.

[7] Worku, A. K.; Ayele, D. W.; Habtu, N. G. Recent advances and future perspectives in engineering of bifunctional electrocatalysts for rechargeable zinc–air batteries. *Mater. Today Adv.* **2021**, *9*, 100116.

[8] Wang, J.; Kong, H.; Zhang, J. Y.; Hao, Y.; Shao, Z. P.; Ciucci, F. Carbon-based electrocatalysts for sustainable energy applications. *Prog. Mater. Sci.* **2021**, *116*, 100717.

[9] Petrie, J. R.; Cooper, V. R.; Freeland, J. W.; Meyer, T. L.; Zhang, Z. Y.; Lutterman, D. A.; Lee, H. N. Enhanced bifunctional oxygen catalysis in strained $LaNiO_3$ perovskites. *J. Am. Chem. Soc.* **2016**, *138*, 2488–2491.

[10] Wei, Y. C.; Weng, Z.; Guo, L. C.; An, L.; Yin, J.; Sun, S. Y.; Da, P. F.; Wang, R.; Xi, P. X.; Yan, C. H. Activation strategies of perovskite-type structure for applications in oxygen-related electrocatalysts. *Small Methods* **2021**, *5*, 2100012.

[11] Zhou, T. P.; Xu, W. F.; Zhang, N.; Du, Z. Y.; Zhong, C. A.; Yan, W. S.; Ju, H. X.; Chu, W. S.; Jiang, H.; Wu, C. Z. et al. Ultrathin cobalt oxide layers as electrocatalysts for high-performance flexible Zn–air batteries. *Adv. Mater.* **2019**, *31*, 1807468.

[12] Tan, Y. Y.; Zhu, W. B.; Zhang, Z. Y.; Wu, W.; Chen, R. Z.; Mu, S. C.; Lv, H. F.; Cheng, N. C. Electronic tuning of confined sub-nanometer cobalt oxide clusters boosting oxygen catalysis and rechargeable Zn–air batteries. *Nano Energy* **2021**, *83*, 105813.

[13] Jiang, R.; Chen, X.; Deng, J. X.; Wang, T. Y.; Wang, K.; Chen, Y. L.; Jiang, J. Z. *In-situ* growth of ZnS/FeS heterojunctions on biomass-derived porous carbon for efficient oxygen reduction reaction. *J. Energy Chem.* **2020**, *47*, 79–85.

[14] Shang, H. S.; Sun, W. M.; Sui, R.; Pei, J. J.; Zheng, L. R.; Dong, J. C.; Jiang, Z. L.; Zhou, D. N.; Zhuang, Z. B.; Chen, W. X. et al. Engineering isolated Mn–N_2C_2 atomic interface sites for efficient bifunctional oxygen reduction and evolution reaction. *Nano Lett.* **2020**, *20*, 5443–5450.

[15] Wang, H.; Li, J. M.; Li, K.; Lin, Y. P.; Chen, J. M.; Gao, L. J.; Nicolosi, V.; Xiao, X.; Lee, J. M. Transition metal nitrides for electrochemical energy applications. *Chem. Soc. Rev.* **2021**, *50*, 1354–1390.

[16] Wu, W. J.; Liu, Y.; Liu, D.; Chen, W. X.; Song, Z. Y.; Wang, X. M.; Zheng, Y. M.; Lu, N.; Wang, C. X.; Mao, J. J. et al. Single copper sites dispersed on hierarchically porous carbon for improving oxygen reduction reaction towards zinc-air battery. *Nano Res.* **2021**, *14*, 998–1003.

[17] Tang, C.; Wang, B.; Wang, H. F.; Zhang, Q. Defect engineering toward atomic Co–N_x–C in hierarchical graphene for rechargeable flexible solid Zn-air batteries. *Adv. Mater.* **2017**, *29*, 1703185.

[18] Liu, J.; Zhang, H.; Qiu, M.; Peng, Z. H.; Leung, M. K. H.; Lin, W. F.; Xuan, J. A review of non-precious metal single atom confined nanomaterials in different structural dimensions (1D–3D) as highly active oxygen redox reaction electrocatalysts. *J. Mater. Chem. A* **2020**, *8*, 2222–2245.

[19] Wei, X.; Zheng, D.; Zhao, M.; Chen, H. Z.; Fan, X.; Gao, B.; Gu, L.; Guo, Y.; Qin, J. B.; Wei, J. et al. Cross-linked polyphosphazene hollow nanosphere-derived N/P-doped porous carbon with single nonprecious metal atoms for the oxygen reduction reaction. *Angew. Chem., Int. Ed.* **2020**, *59*, 14639–14646.

[20] Sun, T. T.; Zhang, P. P.; Chen, W. X.; Wang, K.; Fu, X. Z.; Zheng, T. Y.; Jiang, J. Z. Single iron atoms coordinated to g-C_3N_4 on hierarchical porous N-doped carbon polyhedra as a high-performance electrocatalyst for the oxygen reduction reaction. *Chem. Commun.* **2020**, *56*, 798–801.

[21] Zhang, X. B.; Han, X.; Jiang, Z.; Xu, J.; Chen, L. N.; Xue, Y. K.; Nie, A. M.; Xie, Z. X.; Kuang, Q.; Zheng, L. S. Atomically dispersed hierarchically ordered porous Fe–N–C electrocatalyst for

high performance electrocatalytic oxygen reduction in Zn-air battery. *Nano Energy* **2020**, *71*, 104547.

[22] Zhang, N.; Zhou, T. P.; Chen, M. L.; Feng, H.; Yuan, R. L.; Zhong, C. A.; Yan, W. S.; Tian, Y. C.; Wu, X. J.; Chu, W. S. et al. High-purity pyrrole-type FeN_4 sites as a superior oxygen reduction electrocatalyst. *Energy Environ. Sci.* **2020**, *13*, 111–118.

[23] Martinez, U.; Babu, S. K.; Holby, E. F.; Chung, H. T.; Yin, X.; Zelenay, P. Progress in the development of Fe-based PGM-free electrocatalysts for the oxygen reduction reaction. *Adv. Mater.* **2019**, *31*, 1806545.

[24] Zhao, S. Y.; Chen, G. X.; Zhou, G. M.; Yin, L. C.; Veder, J. P.; Johannessen, B.; Saunders, M.; Yang, S. Z.; De Marco, R.; Liu, C. et al. A universal seeding strategy to synthesize single atom catalysts on 2D materials for electrocatalytic applications. *Adv. Funct. Mater.* **2020**, *30*, 1906157.

[25] Li, X. Y.; Rong, H. P.; Zhang, J. T.; Wang, D. S.; Li, Y. D. Modulating the local coordination environment of single-atom catalysts for enhanced catalytic performance. *Nano Res.* **2020**, *13*, 1842–1855.

[26] Zheng, X. B.; Li, P.; Dou, S. X.; Sun, W. P.; Pan, H. G.; Wang, D. S.; Li, Y. D. Non-carbon-supported single-atom site catalysts for electrocatalysis. *Energy Environ. Sci.* **2021**, *14*, 2809–2858.

[27] Zhang, J. Q.; Zhao, Y. F.; Chen, C.; Huang, Y. C.; Dong, C. L.; Chen, C. J.; Liu, R. S.; Wang, C. Y.; Yan, K.; Li, Y. D. et al. Tuning the coordination environment in single-atom catalysts to achieve highly efficient oxygen reduction reactions. *J. Am. Chem. Soc.* **2019**, *141*, 20118–20126.

[28] Shang, H. S.; Zhou, X. Y.; Dong, J. C.; Li, A.; Zhao, X.; Liu, Q. H.; Lin, Y.; Pei, J. J.; Li, Z.; Jiang, Z. L. et al. Engineering unsymmetrically coordinated $Cu\text{-}S_1N_3$ single atom sites with enhanced oxygen reduction activity. *Nat. Commun.* **2020**, *11*, 3049.

[29] Zhang, J. T.; Zhang, M.; Zeng, Y.; Chen, J. S.; Qiu, L. X.; Zhou, H.; Sun, C. J.; Yu, Y.; Zhu, C. Z.; Zhu, Z. H. Single Fe atom on hierarchically porous S, N-codoped nanocarbon derived from porphyra enable boosted oxygen catalysis for rechargeable Zn-air batteries. *Small* **2019**, *15*, 1900307.

[30] Wang, Y.; Chen, L. H.; Mao, Z. X.; Peng, L. S.; Xiang, R.; Tang, X. Y.; Deng, J. H.; Wei, Z. D.; Liao, Q. Controlled synthesis of single cobalt atom catalysts via a facile one-pot pyrolysis for efficient oxygen reduction and hydrogen evolution reactions. *Sci. Bull.* **2019**, *64*, 1095–1102.

[31] Xia, B. Y.; Yan, Y.; Li, N.; Wu, H. B.; Lou, X. W.; Wang, X. A metal–organic framework-derived bifunctional oxygen electrocatalyst. *Nat. Energy* **2016**, *1*, 15006.

[32] Chen, Y. J.; Gao, R.; Ji, S. F.; Li, H. J.; Tang, K.; Jiang, P.; Hu, H. B.; Zhang, Z. D.; Hao, H. G.; Qu, Q. Y. et al. Atomic-level modulation of electronic density at cobalt single-atom sites derived from metal-organic frameworks: Enhanced oxygen reduction performance. *Angew. Chem., Int. Ed.* **2021**, *60*, 3212–3221.

[33] Yang, J. R.; Li, W. H.; Wang, D. S.; Li, Y. D. Electronic metal–support interaction of single-atom catalysts and applications in electrocatalysis. *Adv. Mater.* **2020**, *32*, 2003300.

[34] Liu, W. P.; Hou, Y. X.; Pan, H. H.; Liu, W. B.; Qi, D. D.; Wang, K.; Jiang, J. Z.; Yao, X. D. An ethynyl-linked Fe/Co heterometallic phthalocyanine conjugated polymer for the oxygen reduction reaction. *J. Mater. Chem. A* **2018**, *6*, 8349–8357.